Sustainable Energy, 2014, Vol. 2, No. 4, 126-133
Available online at http://pubs.sciepub.com/rse/2/4/2

DOI:10.12691/rse-2-4-2

Study of the Reynolds Number Effect on the Aerodynamic Structure around an Obstacle with Inclined Roof

Slah Driss, Zied Driss*, Imen Kallel Kammoun

Laboratory of Electro-Mechanic Systems (LASEM), National School of Engineers of Sfax (ENIS), Univrsity of Sfax, Sfax, TUNISIA
*Corresponding author: zied.driss@enis.rnu.tn

Received July 29, 2014; Revised August 10, 2014; Accepted August 13, 2014

Abstract In this work, we are interested on the study of the Reynolds number effect on the aerodynamic structure around an obstacle with inclined roof. Different Reynolds numbers equals to Re=2666, Re=10666, Re=24000 and Re=32000 are particularly considered. The software "SolidWorks Flow Simulation" has been used to present the local characteristics. The numerical model considered is based on the resolution of the Navier-Stokes equations in conjunction with the standard k-ε turbulence model. These equations were solved by a finite volume discretization method. The numerical model is validated with experimental results conducted on an open wind tunnel equipped by an adequate model.

Keywords: *CFD, modeling, airflow, obstacle, inclined roof, wind tunnel*

Cite This Article: Slah Driss, Zied Driss, and Imen Kallel Kammoun, “Study of the Reynolds Number Effect on the Aerodynamic Structure around an Obstacle with Inclined Roof.” *Sustainable Energy*, vol. 2, no. 4 (2014): 126-133. doi: 10.12691/rse-2-4-2.

1. Introduction

The charactristics of the flows around building-shaped obstacles are different from those in laminar boundary immersed in turbulent boundary layers. It is important for the appropriate estimation of wind loading to investigate these characterestics of flows observed under oncoming turbulence [1,2]. Computational simulations have an advantage to clarify the process and mechanism of these localized phenomena. In recent years, several methods to generate turbulent inflow data were proposed and some of them were used as inflow data [3,4,5]. In this context, Nasrollahei et al. [6] used a builder software to study the thermal and cryogenic performance. The results of the research show that the temperature of Shevaduns in summer is less than the average maximum temperature and the average minimum temperature of outdoor, and the thermal condition of the Shevadun space during the measurement is lower than the thermal comfort limit which is specified in the standard. Ould Said et al. [7] dedicated to the numerical simulation of thermal convection in a two dimensional vertical conical cylinder partially annular space. The governing equations of mass, momentum and energy are solved using the CFD FLUENT code. Tominaga and Stathopoulos [8] reviewed current modeling techniques in computational fluid dynamics (CFD) simulation of near-field pollutant dispersion in urban environments and discussed the findings to give insight into future applications. De Paepe et al. [9] simulated five different wind incidence angles using a turntable, in order to quantify their effect on indoor air velocities. The responses in local air velocities could largely be attributed to the relative position of the end walls of the scale models orientated towards the wind. This crucial position allows the measured air velocity trends to be explained. The estimated airflow rates gradually decreased for larger wind incidence angles. Lim et al. [10] presented a numerical simulation of flow around a surface mounted cube placed in a turbulent boundary layer which, although representing a typical wind environment, to match a series of wind tunnel observations. The simulations were carried out at a Reynolds number, based on the velocity at the cube height, of 20,000. The results presented include detailed comparison between measurements and large eddy simulation (LES) computations of both the inflow boundary layer and the flow field around the cube including mean and fluctuating surface pressures. Melo et al. [11] developed two Gaussian atmospheric dispersion models, AERMOD and CALPUFF. Both incorporating the PRIME algorithm for plume rise and building downwash, are intercompared and validated using wind tunnel data on odour dispersion around a complex pig farm facility comprising of two attached buildings. The results show that concentrations predicted by AERMOD are in general higher than those predicted by CALPUFF, especially regarding the maximum mean concentrations observed in the near field. Comparison of the model results with wind tunnel data showed that both models adequately predict mean concentrations further downwind from the facility. However, closer to the buildings, the models may over-predict or under-predict concentrations by a factor of two, and in certain cases even larger, depending on the conditions. Meslem et al. [12] observed changes in the prediction of local and global mean-flow quantities as a function of the considered turbulence model and by the lack of consensus in the literature on their performance to predict jet flows with significant three-dimensionality. The study reveals that none of the turbulence models is able to predict well all jet characteristics in the same time. Reynolds stress turbulence model leads to a better agreement between the numerical results and the experimental data for the local jet flow expansion, whereas global flow expansion and ambient air induction are better predicted by the shear stress transport k-ω turbulence model. All linear (Low Reynolds and Renormalization Group) and nonlinear (quadratic and cubic) k-ε turbulence models overestimate local and global expansions and ambient air induction. The k-ω turbulence model underestimates on one hand the global expansion and the ambient air induction and on the other hand the transverse jet deformation is not well predicted. The turbulence kinetic energy increases unrealistically in the jet near field for all k-ε turbulence models and Reynold's Stress Models (RSM). In this region shear-stress transport (SST) k-ω model was in close agreement with measurements. Ntinas et al. [13] predicted the airflow around buildings is challenging due to the dynamic characteristics of wind. A time-dependent simulation model has been applied for the prediction of the turbulent airflow around obstacles with arched and pitched roof geometry, under wind tunnel conditions. To verify the reliability of the model an experiment was conducted inside a wind tunnel and the air velocity and turbulent kinetic energy profiles were measured around two small-scale obstacles with an arched-type and a pitched-type roof. Luo et al. [14] studied models of cuboid obstacles to characterize the three-dimensional responses of airflow behind obstacles with different shape ratios to variations in the incident flow in a wind-tunnel simulation. Wind velocity was measured using particle image velocimetry (PIV). The flow patterns behind cuboid obstacles were complicated by changes in the incidence angle of the approaching flow and in the obstacle's shape ratio. Gousseau et al. [15] used Large-Eddy Simulation (LES) to investigate the turbulent mass transport mechanism in the case of gas dispersion around an isolated cubical building. Close agreement is found between wind-tunnel measurements and the computed average and standard deviation of concentration in the wake of the building. A detailed statistical analysis of these variables is performed to gain insight into the dispersion process. In particular, the fact that turbulent mass flux in the stream wise direction is directed from the low to high levels of mean concentration (counter-gradient mechanism) is explained. The large vortical structures developing around the building are shown to play an essential role in turbulent mass transport Smolarkiewicz et al. [16] performed large-eddy simulations (LES) of the flow past a scale model of a complex building. Calculations are accomplished using two different methods to represent the edifice. The results demonstrated that, contrary to popular opinion, continuous mappings such as the Gal-Chen and Somerville transformation are not inherently limited to gentle slopes. Calculations for a strongly stratified case are also presented to point out the substantial differences from the neutral boundary layer flows. Ahmad et al. [17] provided a comprehensive literature on wind tunnel simulation studies in urban street canyons/intersections including the effects of building configurations, canyon geometries, traffic induced turbulence and variable approaching wind directions on flow fields and exhaust dispersion. Jiang et al. [18] studied three ventilation cases, single-sided ventilation with an opening in windward wall, single-sided ventilation with an opening in leeward wall, and cross ventilation. In the wind tunnel, a laser Doppler anemometry was used to provide accurate and detailed velocity data. In LES calculations, two subgrid-scale (SS) models, a Smagorinsky SS model and a filtered dynamic SS model, were used. The numerical results from LES are in good agreement with the experimental data, in particular with the predicted airflow patterns and velocities around and within, and the surface pressures over, the models.

According to these anteriors studies, it's clear that the study of the aerodynamic around the obstacle is very interesting. Indeed, the literature review confirms that there is a paucity on the inclined roof obstacle study. For thus, we are interested on the study of the Reynolds number effect.

2. Geometrical System

The computational domain is shown in Figure 1. It is defined by the interior volume of the wind tunnel blocked by two planes. The first one is in the tranquillization chamber entry and the second one is in the exit of the diffuser. The test vein is equipped by the considered inclined roof obstacle.

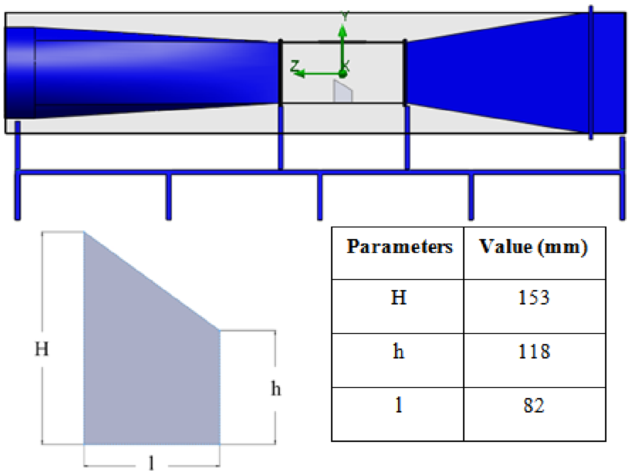

Parameters	Value (mm)
H	153
h	118
l	82

Figure 1. Geometrical arrangement

3. Numerical Model

The software "SolidWorks Flow Simulation" has been used to present the local characteristics. The numerical model considered is based on the resolution of the Navier-Stokes equations in conjunction with the standard k-ε turbulence model. These equations were solved by a finite volume discretization method [19,20,21].

3.1. Boundary Conditions

The boundary condition is required any where fluid enters the system and can be set as a pressure, mass flow, volume flow or velocity. Since we study in this application the effect of Reynolds number, we will give different values to the inlet velocity. For the outlet pressure we take a value of 101325 Pa which means that at this opening the fluid exits the model to an area of an atmospheric pressure. Knowing that the obstacle is suspended in our domain, both the roof top obstacle and the wall of our domain are considered as a wall boundary condition.

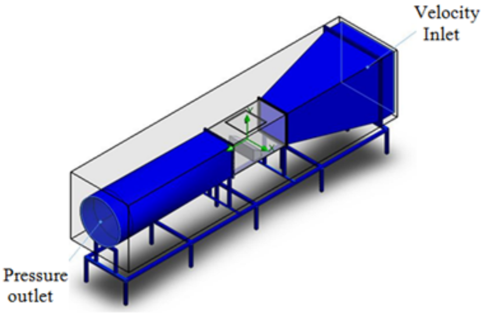

Reynolds number Re	Velocity inlet V (m.s^{-1})	Pressure outlet p (Pa)
2 666	**0.1**	**101325**
10 666	**0.4**	**101325**
24 000	**0.9**	**101325**
32 000	**1.2**	**101325**

Figure 2. Boundary conditions

3.2. Mesh Resolution

Figure 3 shows the initial mesh of the model. It is named initial since it is the mesh that the calculation starts from and it could be further refined during the calculation if the solution-adaptive meshing is enabled. The initial mesh is constructed from the basic mesh by refining the basic mesh cells in accordance with the specified mesh settings. The basic mesh is formed by dividing the computational domain into slices by parallel planes which are orthogonal to the global coordinate system's axes. Flow simulation options permit the computational mesh adjustment. In the near wall of roof top obstacle, the "initial" mesh corresponds to a cell of 5 cm. However, the "refined" mesh corresponds to a cell of 0.5 cm. In these cases, the number of hexahedral cells is respectively equal to 5621 and 37038.

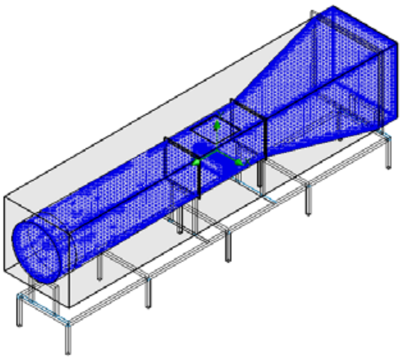

Figure 3. Meshing

4. Numerical Results

4.1. Magnitude Velocity

Figure 4 presents the distribution of the magnitude velocity in the longitudinal planes defined by X=0 mm. According to these results, it has been noted that the velocity is weak in the inlet of the collector. It is indeed governed by the boundary condition values of the inlet velocity. In this region, the velocity field is found to be uniform and increases progressively downstream of the collector. At the test vein, an important increase has been noted due to the reduction of the tunnel section that causes the throttling of the flow. While the upper side of the obstacle is characterized by the high velocity, a brutal drop is located behind the obstacle and this is due to the deceleration of the velocity field while passing through the obstacle. In the test vein, the velocity keeps increasing till the out of the test section. Then, a decrease has been noted through the diffuser where the minimum velocity values are recorded in the lateral walls of the diffuser. Indeed, it's clear that the Reynolds number has a direct effect on the increase of the maximum value of the velocity. For example, with Re=2666 the maximum value of the velocity is equal to V=0.88 m.s^{-1}. However, with Re= 32000 the maximum value of the velocity is equal to V=10.49 m.s^{-1}.

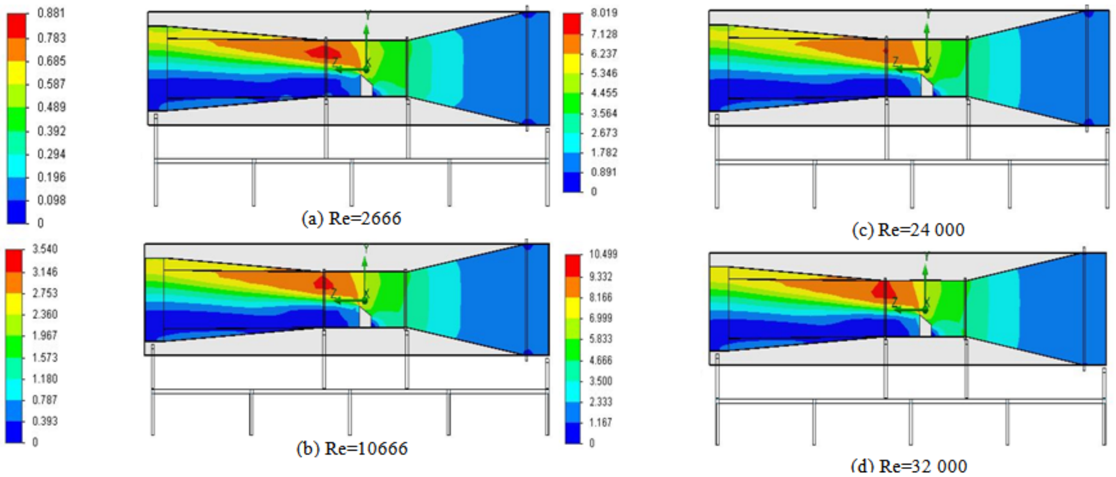

(a) Re=2666

(c) Re=24 000

(b) Re=10666

(d) Re=32 000

Figure 4. Velocity in the longitudinal plane X=0 m

4.2. Velocity Streamlines

Figure 5 presents the distribution of the velocity streamlines in the longitudinal plane defined by X=0 mm. According to these results, it has been noted that the velocity is weak in the inlet of the collector. It is indeed governed by the boundary condition value of the inlet velocity. In this region the velocity is found to be uniform and increases progressively downstream of the collector. At the test vein, an important increase has been noted due to the reduction of the tunnel section that causes the throttling of the flow. While the upper side of the obstacle is characterized by the high velocity, a brutal drop is located behind the obstacle. This is due to the deceleration of the velocity field while passing by the obstacle. In the test vein the velocity keeps increasing till the out of the test section. Then, a decrease on the maximum values has been noted through the diffuser where the minimum velocity values are recorded in the lateral walls of the diffuser. The flow circulation appears in the dead zones where the velocity presents a weak value. In our case, the flow circulations are located behind the obstacle and in the diffuser outlet. Besides, the maximum value of the velocity streamlines increases with the increase of Reynolds number value.

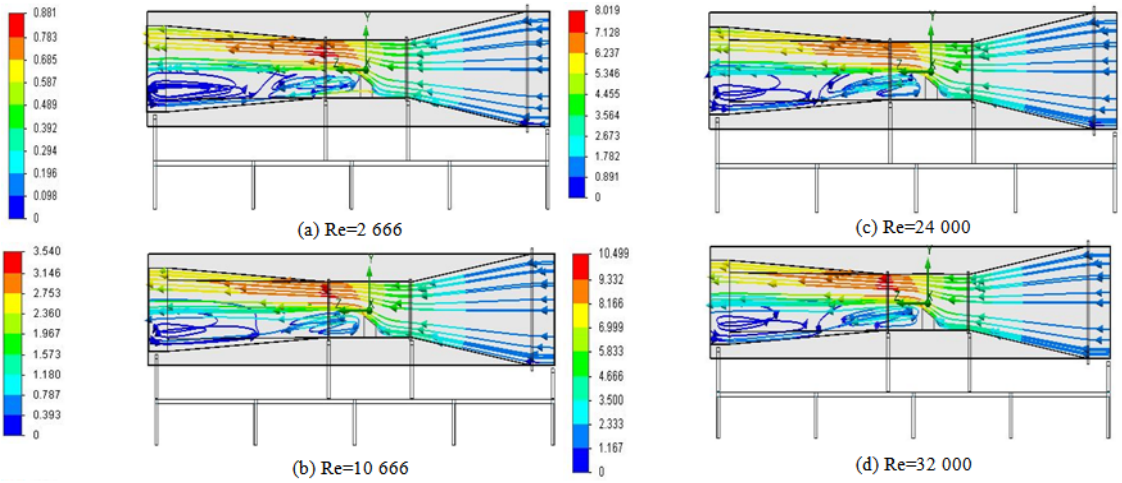

(a) Re=2 666

(c) Re=24 000

(b) Re=10 666

(d) Re=32 000

Figure 5. Velocity streamlines in the longitudinal plane x=0 mm

4.3. Static Pressure

Figure 6 presents the distribution of the static pressure in the longitudinal planes defined by X=0 mm. According to these results, it can easily be noted that the total pressure is on its maximum in the inlet of the collector. Besides, it has been observed a depression above the obstacle. The pressure continues decreasing the way out of the test vein. A brutal drop of the pressure has been noted just behind the obstacle. The distribution of the static pressure in the plane y=0 mm shows that a depression zone is located in the second half of the wind tunnel through the diffuser. Indeed, it's clear that the Reynolds number has a direct effect on the static pressure distribution. In fact, the maximum value of the static pressure increases with the increase of the Reynolds number value. For example, in the longitudinal plane X=0, the maximum value of the static pressure is equal to p=101325 Pa for Re=2666 and becomes equal to p=101372 for Re= 32000.

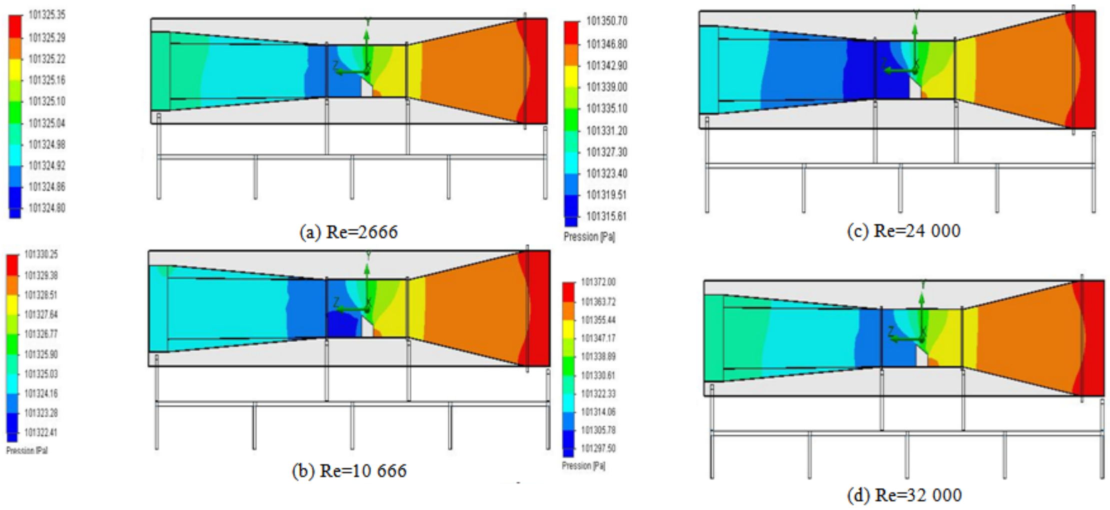

(a) Re=2666

(c) Re=24 000

(b) Re=10 666

(d) Re=32 000

Figure 6. Static pressure in the longitudinal plane X=0 mm

4.4. Dynamic Pressure

Figure 7 presents the distribution of the dynamic pressure respectively in the longitudinal planes defined by X=0 mm According to these results, the dynamic pressure is found to be weak in the collector inlet and increases gradually through the collector as long as the tunnel section gets smaller. When it gets to the test section, the dynamic pressure keeps increasing in the upstream of the obstacle. A compression zone is recorded in the region located behind the obstacle and is developed through the diffuser. The distribution of the dynamic pressure in the transverse plane shows a minimum zone located in the downside of the wind tunnel and a maximum zone located in its upper side. Indeed, it’s clear that the Reynolds number has a direct effect on the distribution of the dynamic pressure. In fact, the maximum value of the dynamic pressure increases with the increase of Reynolds number value. For example, at longitudinal plane X=0 mm, the maximum value of the dynamic pressure is equal to p_d=0.43 Pa for the Reynolds number equal to Re= 2666. However, it becomes equal to p_d=60 Pa for the Reynolds number equal to Re=32000.

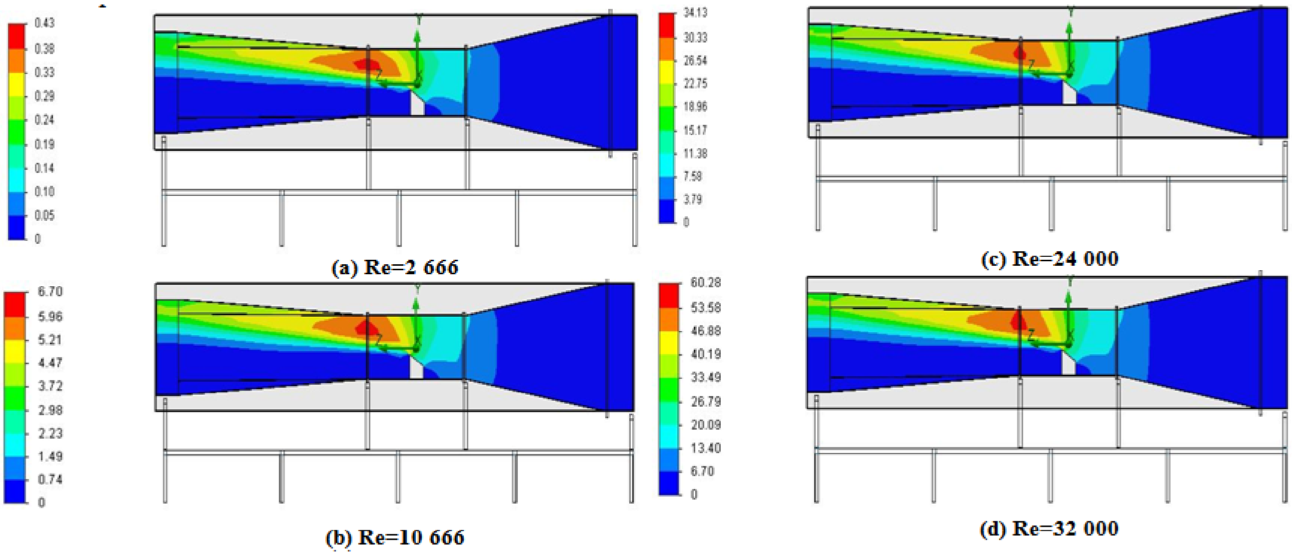

(a) Re=2 666

(c) Re=24 000

(b) Re=10 666

(d) Re=32 000

Figure 7. Dynamic pressure in the longitudinal plane X=0 mm

4.5. Turbulent Kinetic Energy

Figure 8 presents the distribution of the turbulent kinetic energy in the longitudinal plane defined by X=0 mm. From these results, it has been noted that the turbulent kinetic energy is found to be very weak in the first half of the wind tunnel in the obstacle upstream. A wake characteristic of the maximum value of the turbulent kinetic energy appears upstream of the obstacle. This wake starts in the obstacle corner until the outlet of the diffuser. Indeed, it’s clear that the Reynolds number has a direct effect on the turbulent kinetic energy distribution. In fact, the maximum value of the turbulent kinetic energy increases with the increase of the Reynolds number value. For example, in the longitudinal plane X=0 mm, the maximal value of the turbulent kinetic energy is equal to k=0.03 $m^2.s^{-2}$ for a Reynolds number equal to Re=2666. However, it becomes equal to k=4.44 $m^2.s^{-2}$ for a Reynolds number equal to Re= 32000.

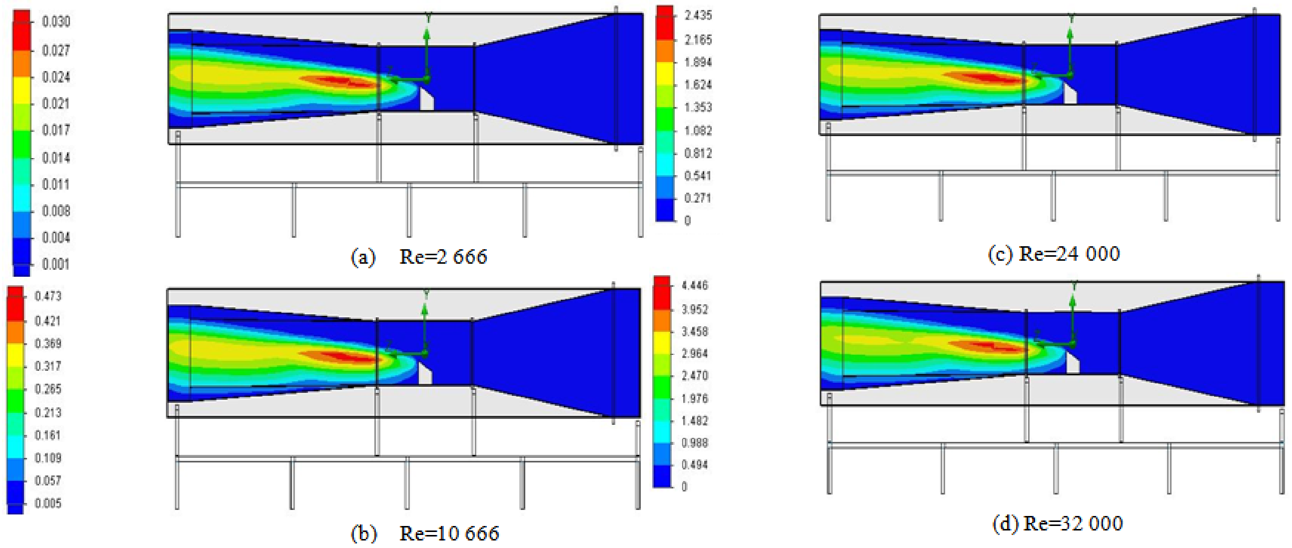

(a) Re=2 666

(c) Re=24 000

(b) Re=10 666

(d) Re=32 000

Figure 8. Turbulent kinetic energy in the longitudinal plane X=0 mm

4.6. Turbulent Dissipation Rate

Figure 9 presents the distribution of the turbulent dissipation rate on the longitudinal plans defined by X=0 mm. From these results, it has been noted that the turbulent dissipation rate is found to be very weak in the first half of the wind tunnel in the obstacle upstream. A wake characteristic of the maximum value of the turbulent dissipation rate appears upstream of the obstacle. This wake starts in the obstacle corner until the outlet of the diffuser. Indeed, it’s clear that the Reynolds number has a direct effect on the turbulent dissipation rate distribution.

In fact, the maximum value of the turbulent dissipation rate increases with the increase of the Reynolds number value. For example, in the longitudinal plane X=0 mm, the maximal value of the turbulent dissipation rate is equal to ε=0.04 W/Kg for a Reynolds number equal to Re=2666. However, it becomes equal to ε=72.2 W/Kg for a Reynolds number equal to Re= 32000.

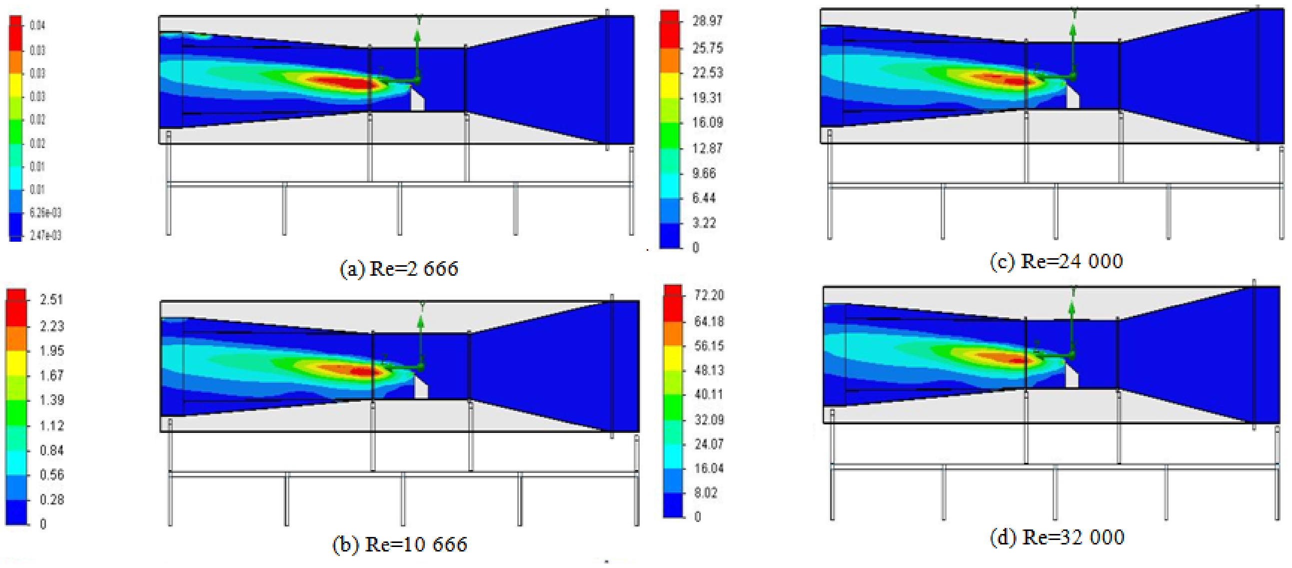

(a) Re=2 666

(c) Re=24 000

(b) Re=10 666

(d) Re=32 000

Figure 9. Turbulent dissipation rate in the longitudinal plane x=0 mm

4.7. Turbulent Viscosity

Figure 10 presents the distribution of the turbulent viscosity in the longitudinal planes defined by X=0 mm. According to thes results; it’s clear that the viscosity is at its minimum in the collector region but starts increasing after crossing the obstacle. Its maximum is located in the outlet of the diffuser. Indeed, it’s clear that the Reynolds number has a direct effect on the turbulent viscosity. In fact, the maximum value of the turbulent viscosity increases with the increase of the Reynolds number value. For example, in the longitudinal plane X=0 mm, the maximal value of the turbulent viscosity is equal to μ_t=0.005 Pa.s for a Reynolds number equal to Re=2666. However, it becomes equal to μ_t=0.06 Pa.s for a Reynolds number equal to Re= 32000.

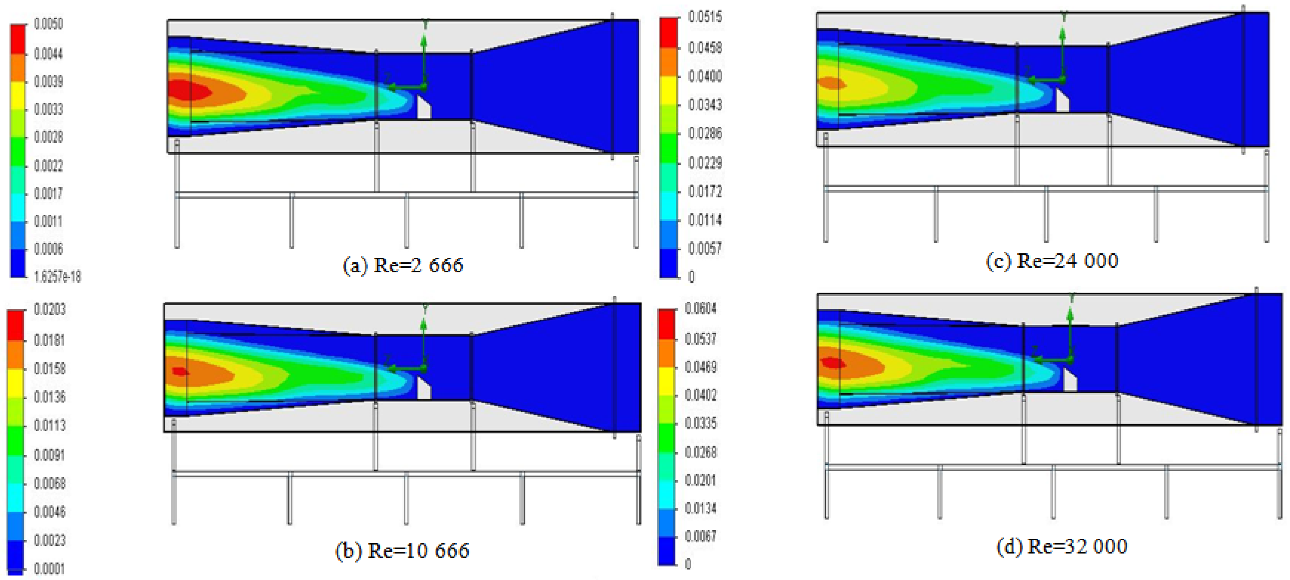

(a) Re=2 666

(c) Re=24 000

(b) Re=10 666

(d) Re=32 000

Figure 10. Turbulent viscosity in the longitudinal plane X=0 mm

4.8. Vorticity

Figure 11 presents the distribution of the vorticity respectively in the longitudinal plane defined by x=0 mm. According to these results, the vorticity is at its minimum in the collector region and starts increasing after crossing the obstacle. The greatest vorticity values are reached after hitting the obstacle blade. Indeed, it’s clear that the Reynolds number has a direct effect on the vorticity distribution. In fact, the maximum value of the vorticity increases with the increase of the Reynolds number value. For example, in the longitudinal plane X=0 mm, the maximal value of the vorticity is equal to 6.2 s^{-1} for a Reynolds number equal to Re=2666. However, it becomes equal to V=96.5 s $^{-1}$ for a Reynolds number equal to Re= 32000.

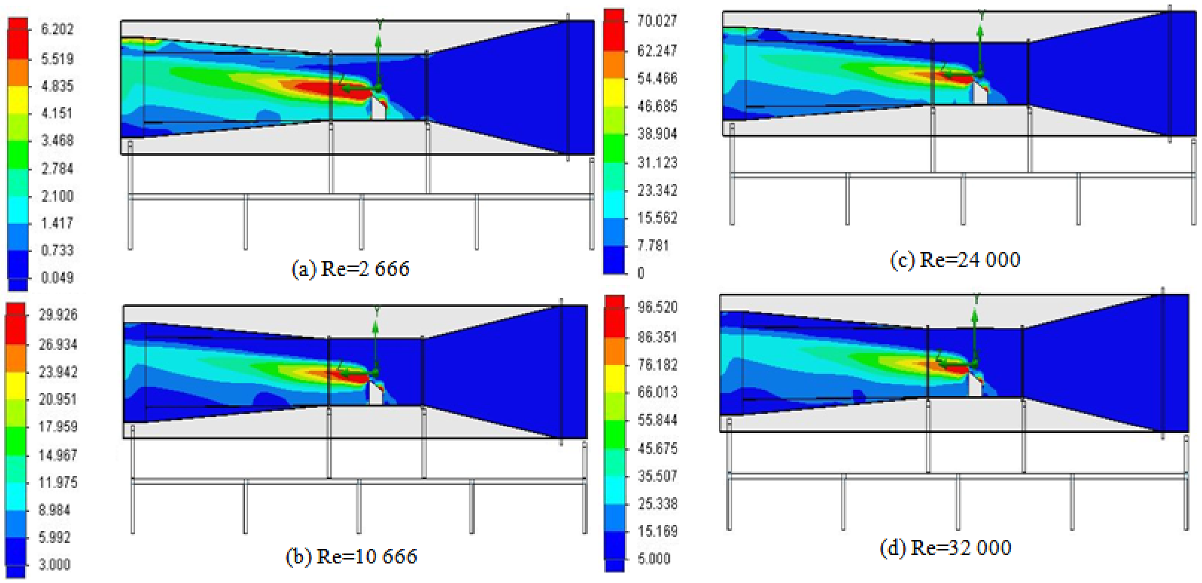

Figure 11. Vorticity in the longitudinal plane X=0 mm

5. Comparison with Experimental Results

In this section, we are interested on the comparison of the numerical results with the experimental results conducted in the LASEM laboratories using a wind tunnel (Figure 12). The velocity profiles are chosen for points situated in the test section. The considered planes are defined by Z=0 mm, Z=150 mm and Z=-150 mm. The results for each plane are shown respectively in Figure 13. For each transverse plane, values are taken along the directions defined by X=0 mm. Near the obstacle, it's clear that the velocity value is very weak. Outside, the velocity has a maximum value. Indeed, it's clear that the Reynolds number has a direct effect on the maximum value. For example, for the direction defined by Z=0 mm and X=0 mm, the maximum value is equal to V=0.6 m.s^{-1} for the Reynolds number equal to Re= 2666. However, this value increases to V=7 m.s^{-1} for the Reynolds number equal to Re=32000. The comparison between the numerical and experimental velocity values leads us to the conclusion that despite some unconformities, the values are comparable. The numerical model seems to be able to predict the aerodynamic characteristics of the air flow around the inclined roof obstacle.

Figure 12. Wind tunnel equipped by an inclined roof obstacle

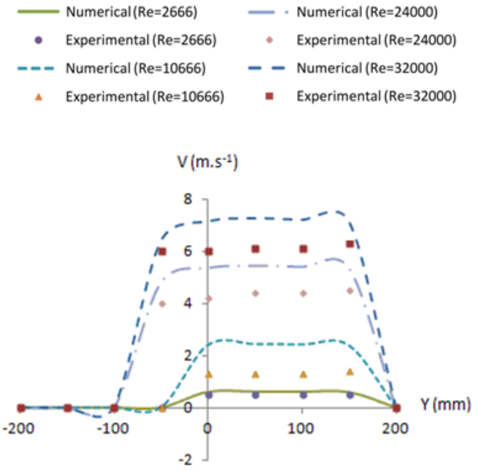

(a) Z=0 mm and X=0 mm

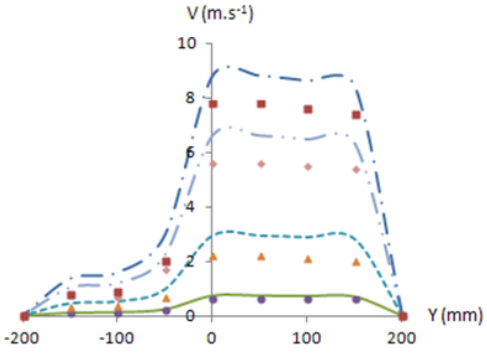

(b) Z=-150 mm and X=0 mm

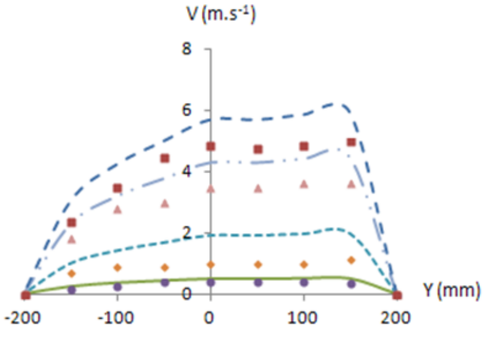

(c) Z=150 mm and X=0 mm

Figure 13. Velocity profiles

6. Conclusion

In this paper, we have performed a numerical simulation to study the Reynolds number effect on the aerodynamic characteristics around an obstacle with inclined roof. Numerical results, such as velocity fields, pressure and turbulent characteristics are presented in the wind tunnel, considered as a control volume. According to the obtained results, it has been noted that the Reynolds number has a direct effect on the local characteristics. In fact, the maximum values of the velocity and the turbulent characteristics increase with the increase of the Reynolds number. Indeed, the circulation zones of the velocity streamlines and the wakes characteristics of the maximum values of the turbulent characteristics are located after hitting the obstacle. Use of this knowledge will assist the design of packaged installations of the wind rotors in the buildings. In the future, we propose to study the geometrical effect of the obstacle.

Nomenclature

H: big high, m
h: small high, m
k: turbulent kinetic energy, J.kg^{-1}
l: length, m
p: pressure, Pa
Re: Reynolds number, dimensionless
t: time, s
V: magnitude velocity, m.s^{-1}
X: Cartesian coordinate, m
Y: Cartesian coordinate, m
Z: Cartesian coordinate, m
ε: dissipation rate of the turbulent kinetic energy, W.kg^{-1}
μ_t: turbulent viscosity, Pa.s

References

[1] Nozawa, K., Tamura, T., *Large eddy simulation of the flow around a low-rise building immersed in a a rough-wall turbulent boundary layer*, J. Wind Eng. Ind. Aerodyn., 90. 1151-1162. 2002.

[2] Kawai, H., *Local peak pressure and conical vortex on building, Proceedings of the 10th International Conference on Wind Engineering.* 1807-1812. 1999.

[3] Kondo, K., Murakami, S., Mochida, A., *Generation of velocity fluctuation for inflow boundary condition of LES,* J. Wind Eng. Ind., 67&68. 51-64. 1997.

[4] Kataoka, H., Mizuno, M., *Numerical flow computation around 3D square cylinder using inflow turbulence,* J. Archit. Plan environ. Eng., AIJ 523. 71-77. 1999.

[5] Noda, H., Nakayama, A., *Reproducibility of flow past two-dimensional rectangular cylinders in a homogeneous turbulent flow by LES,* J. Wind Eng., 89. 321-324. 2001.

[6] Nasrollahei, N., Mahdavinejad, M., Hadiyanpour, M., *Studying the Thermal and Cryogenic Performance of Shevadun in Native (Local) Buildings of Dezful Based on Modeling and Environmental Measuring,* American Journal of Energy Research, 1 (3). 45-53. 2013.

[7] Ould said, B., Retiel, N., Bouguerra, E.H., *Numerical Simulation of Natural Convection in a Vertical Conical Cylinder Partially Annular Space,* American Journal of Energy Research, 2 (2). 24-29. 2014.

[8] Tominaga, Y., Stathopoulos, T., *CFD simulation of near-field pollutant dispersion in the urban environment: A review of current modeling techniques,* Atmospheric Environment, 79. 716-730. 2013.

[9] De Paepe, M., Pieters, J. G., Cornelis, W. M., Gabriels, D., Merci, B., Demeyer, P., *Airflow measurements in and around scale-model cattle barns in a wind tunnel: Effect of wind incidence angle,* Biosystems Engineering 115, 211-219. 2013.

[10] lim, H.C., Thomas, T.G., Castro, I.P., *Flow around a cube in a turbulent boundary layer: LES and experiment,* Journal of Wind Engineering and Industrial Aerodynamics, 97. 96-109. 2009.

[11] De Melo, A. M. V., Santos, J. M., Mavrroidis, I., Reis Junior, N. C., *Modelling of odour dispersion around a pig farm building complex using AERMOD and CALPUFF. Comparison with wind tunnel results,* Building and Environment, 56. 8-20. 2012.

[12] Meslema, A., Bode, F. Croitorub, Cristiana C., *Comparison of turbulence models in simulating jet flow from a cross-shaped orifice,* European Journal of Mechanics B/Fluids, 44. 100-120. 2014.

[13] Ntinas, G.K., Zhangb, G., Fragos, V.P., Bochtis, D.D., Nikita-Martzopoulou, Ch., *Airflow patterns around obstacles with arched and pitched roofs: Wind tunnel measurements and direct simulation,* European Journal of Mechanics B/Fluids, 43. 216-229. 2014.

[14] Luo, W., Dong, Z., Qian, G., Lu, J., *Wind tunnel simulation of the three-dimensional airflow patterns behind cuboid obstacles at different angles of wind incidence and their significance for theformation of sand shadows,* Geomorphology, 139-140. 258-270. 2012.

[15] Gousseau, P., Blocken, B., Van Heijst, G.J.F., Large-Eddy Simulation of pollutant dispersion around a cubical building, *Analysis of the turbulent mass transport mechanisim by unsteady concentration and velocity statistics,* Environmental pollution, 167. 47-57. 2012.

[16] Piotr, K.S., Sharman, R., Weil, J., Steven G. Perry, Heist, D., Bowker, G., *Building resolving large-eddy simulations and comparison with wind tunnel experiments,* Journal of Computational Physics, 227. 633-653. 2007.

[17] Ahmed, K., Khare, M., Chaudhry, K.K. *Wind tunnel simulation studies on dispersion at urban street canyons and intersections- a review,* J. Wind Eng. Ind. Aerodyn., 93. 697-717. 2005.

[18] Jiang, Y., Alexander, D., Jenkins, Huw. Rob Arthur, Qingyan Chen, Natural ventilation in buildings: *measurement in a wind tunnel and numerical simulation with large-eddy simulation,* Journal of Wind Engineering and Industrial Aerodynamics, 91. 331-353. 2003.

[19] Driss, Z., Bouzgarrou, G., Chtourou, W., Kchaou, H., Abid, M.S., *Computational studies of the pitched blade turbines design effect on the stirred tank flow characteristics*, European Journal of Mechanics B/Fluids, 29. 236-245. 2010.

[20] Ammar, M., Chtourou, W., Driss, Z., Abid, M.S., *Numerical investigation of turbulent flow generated in baffled stirred vessels equipped with three different turbines in one and two-stage system,* Energy, 36. 5081-5093. 2011.

[21] Driss, Z., Abid, M.S., *Use of the Navier-Stokes Equations to Study of the Flow Generated by Turbines Impellers.* Navier-Stokes Equations: Properties, Description and Applications, 3. 51-138. 2012.